# Nernst coefficient measurements in twodimensional materials

Qi Feng $^{1,2,5}$ , Tianhui Zhu $^{3,5}$ , Yu Jian $^{1,2}$ , Wei Yuan $^{1,2}$ , Huimin Peng $^{1,2}$ , Jinrui Zhong $^{1,2}$ , Junxi Duan $^{1,2,*}$  and Mona Zebarjadi $^{3,4}$ 

1 Key Laboratory of Advanced Optoelectronic Quantum Architecture and Measurement (MOE), School of Physics, Beijing Institute of Technology, Beijing, People's Republic of China

2 Micronano Center, Beijing Key Laboratory of Nanophotonics & Ultrafine Optoelectronic Systems, Beijing Institute of Technology, Beijing, People's Republic of China

3 Department of Electrical and Computer Engineering, University of Virginia, Charlottesville, VA 22932, United States of America

4 Department of Materials Science and Engineering, University of Virginia, Charlottesville, VA 22932, United States of America

E-mail: junxi.duan@bit.edu.cn

#### **Abstract**

The discovery of two-dimensional (2D) ferromagnets and antiferromagnets with topologically nontrivial electronic band structures makes the study of the Nernst effect in 2D materials of great importance and interest. To measure the Nernst coefficient of 2D materials, the detection of the temperature gradient is crucial. Although the microfabricated metal wires provide a simple but accurate way for temperature detection, a linear-response assumption that the temperature gradient is a constant is still necessary and has been widely used to evaluate the temperature gradient. However, with the existence of substrates, this assumption cannot be precise. In this study, we clearly show that the temperature gradient strongly depends on the distance from the heater by both thermoelectric transport and thermoreflectance measurements. Fortunately, both measurements show that the temperature gradient can be well described by a linear function of the distance from the heater. This linearity is further confirmed by comparing the measured Nernst coefficient to the value calculated from the generalized Mott's formula. Our results demonstrate a precise way to measure the Nernst coefficient of 2D materials and would be helpful for future studies.

**Keywords:** Nernst coefficient, two-dimensional materials, thermoelectric transport, thermoreflectance

## 1. Introduction

Thermally driven electron transport in ferromagnet can generate a transverse voltage drop, called anomalous Nernst effect (ANE). Similar to anomalous Hall effect, ANE is closely related to the topology of the electronic band structure [1–3]. Recently, large ANE has been observed in ferromagnetic semimetals and chiral antiferromagnets [4–9]. These observations not only deepen the understanding of the topological origin of ANE, but also trigger renewed interest in potential applications [9–11]. The transverse nature of the Nernst effect can decouple the electrical-thermal correlation and avoid the contact-resistance problem, providing a potential pathway to surpass the conventional thermoelectrics. While the integration of Berry curvature of occupied bands determines the AHE, ANE is closely related to the Berry curvature at  $E_F$ . The gate tunability of  $E_F$  in two-dimensional (2D) materials thus provides excellent opportunities [12–15]. Together with the discovery of 2D ferromagnets and antiferromagnets with topologically nontrivial electronic band structures, the study of Nernst effect in 2D materials is of great importance and interest [16, 17].

To measure the Nernst coefficient of 2D materials, it is crucial to determine the temperature gradient accurately. In bulk materials, the setup sketched in figure 1(a) is commonly implemented [18, 19]. With the thermometers measuring the temperatures on the two ends of the material, Nernst measurements can be simultaneously done with Seebeck measurements, taking the fact that the thermal transport is one-

dimensional that the temperature gradient is uniform along the material. The temperature gradient can be deduced by  $\nabla T = \frac{\Delta T}{L}$ , where  $\Delta T$  and L are the temperature difference and distance between the hot and cold ends, respectively. In 2D materials, due to the microsize of the flakes, conventional thermometers are no longer applicable. A standard device geometry shown in figure  $\underline{1}(b)$  was proposed and has been widely used  $\underline{15}$ ,  $\underline{20}$ – $\underline{26}$ ]. With the four-probe metal wires (TM1 and TM2 in figure  $\underline{1}(b)$ ) prepared by microfabrication, local temperatures on the two ends of the flake can be accurately measured. In previous Nernst measurements, a linear-repsonse approximation that the thermal transport is one-dimensional and the temperature gradient is a constant has been conventionally adopted to evaluate the temperature

gradient. Under this approximation, the average temperature gradient is  $\frac{\Delta T}{L}$ . However, due to the existence of the substrate, the thermal transport can no longer be taken as one-dimensional as in the bulk case. Although suspending flakes can solve this issue, the need for highly sophisticated bridge structures greatly hampers wide applications.

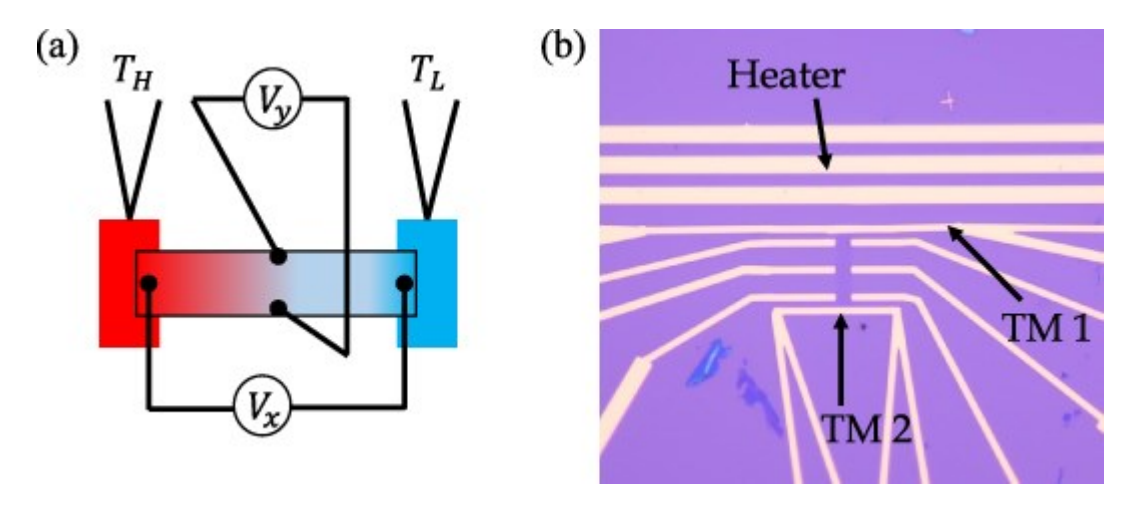


**Figure 1.** Typical measurement setup for macroscopic and microscopic devices. (a) For macroscopic devices, the sample is placed in vacuum with the two ends attached to the heating stage ( $T_H$ ) and cold sink ( $T_L$ ), respectively. The longitudinal and transverse electrodes can measure the Seebeck and Nernst voltages simultaneously. (b) A standard geometry is widely used for thermoelectric measurements on microscopic devices. The thick gold wires on one end of the device serve as the heater. TM1 and TM2 are two thin wires which can monitor the local temperature by four-probe measurements.

In this work, we systematically investigate the evaluation of temperature gradient in Nernst coefficient measurements in 2D materials. With thermoelectric transport and thermoreflectance measurements, the distribution of temperature gradient is clearly shown to be non-uniform on the substrate. The temperature gradient on the end of the channel close to the heater can be twice as large as the value on the far end. Fortunately,

both measurements demonstrate that the temperature gradient along the channel can be well described by a linear function of the distance from the heater. This linearity is further confirmed by comparing the measured Nernst coefficient to the value calculated from the generalized Mott's formula. Our results show that, although the temperature gradient is not uniform and is difficult to be probed locally, the Nernst coefficient can still be measured with the standard geometry by taking the linear dependence into the temperature gradient calculation. Our study would be helpful for future studies of the Nernst effect in 2D materials.

## 2. Methods

The thermoelectric measurements were performed in a Physical Properties Measurement System (Quantum Design, Dynacool) with the chamber pressure maintained below  $10^{-5}$  mbar. The temperature of the device can be well controlled. To measure the Nernst voltage, standard lock-in technique was implemented. A heating current with a frequency of  $f=1.777\,\mathrm{Hz}$  was applied to the heater while the Nernst voltage was detected under 2f. When heating current was applied across the heater, the temperature of the device on the heater side would be increased. Two thermometers, TM1 and TM2, were connected to the device on the two ends. The four-probe resistance of the thermometer is very sensitive to the local temperature and could be used to indicate the temperature change after calibration.

The thermoreflectance technique utilizes the fact that the refractive index and therefore the reflectivity R of a material depends on its temperature T. A so-called

thermoreflectance coefficient,  $C_{TR}$ , is defined to describe this relation:  $C_{TR} = \frac{1}{R_0} \frac{\Delta R}{\Delta T}$ , where  $R_0$  is the initial reflectivity without thermal excitation. The material surface, the incident light wavelength, and the ambient temperature all contribute to  $C_{TR}$ . When  $C_{TR}$  is known, an absolute temperature map of the sample can be obtained based on how the reflectivity changes. During a typical transient measurement with our thermoreflectance imaging system from Microsanj LLC, a voltage pulse with a 5 V bias of duration of 5 ms and 30% duty cycle was applied to turn on the heater. It was synchronized with the light pulse so that the changes in the reflected light intensity when the device is on and off are captured by a charge-coupled (CCD) camera for temperature mapping at a certain delay time. The heating on the sample surface should have reached a steady-state by the end of the voltage pulse and a temperature map at this instant was acquired by averaging over hundreds of thermal excitation cycles. The resolution is diffraction-limited and is about 440 nm under the  $100 \times$  objective and the 530 nm green light.  $C_{TR}$  of  $-2.5 \times 10^{-4}$  is used for the Au

In current study, we have prepared three graphite devices (GN1–GN3), two WTe<sub>2</sub> devices (WTN1, WTN2), and two bare substrates with gold wires/film (EN1, EN2). We have performed thermoelectric measurements in GN1, GN3, WTN1, and WTN2. Thermoreflectance measurements have been done in GN2, EN1, and EN2.

electrodes to accurately extract  $\Delta T$ .

## 3. Results and discussion

We first present the thermoelectric transport results from graphite flakes which have large Nernst coefficient. The thickness of the graphite flakes is chosen to be around 10 nm, ensuring the homogeneity of the channel. The devices are designed similar to the standard geometry with a heater on one end of the flake. Multiple pairs of transverse electrodes are prepared along the channels. Figure 2(a) is the optical image of a typical device, GN1. The results presented below are from this device measured at 300 K. Several devices have been prepared and measured. They all show similar results. We have also done measurements at different temperatures and got consistent results (see supplementary material).

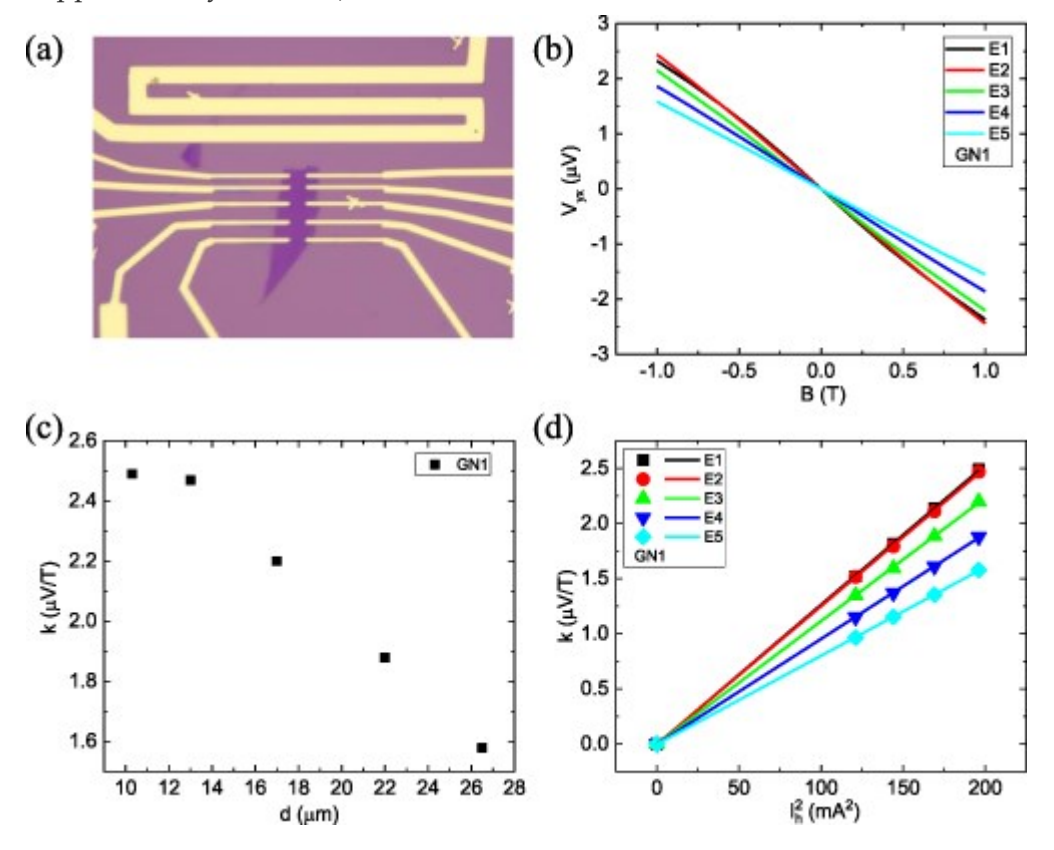


**Figure 2.** Thermoelectric transport results. (a) Optical image of device GN1. The device has multiple transverse electrodes, E1–E5 counted from the heater, to detect the Nernst voltage at different locations. (b) Magnetic field dependence of Nernst voltages measured by different pairs of transverse electrodes. (c) The position dependence of the coefficient k. (d) The coefficient k shows a very good linear dependence on the heating power of the heater.

The Nernst voltage can be expressed as  $V_y = N_{yx}wB \cdot \nabla_x T$ , where  $N_{yx}$  is the Nernst coefficient, W the channel width, B the external magnetic field, and  $\nabla_x T$  the local temperature gradient where the Nernst voltage is measured. In our devices, the

channel has been designed and fabricated to have the same width along the channel. In addition, considering that the graphite flake is 10 nm thick, the Nernst coefficient is uniform along the channel. Therefore, the measured Nernst voltage linearly depends

on the magnetic field,  $V_y = k \cdot B$ , with the coefficient  $k = N_{yx}w \cdot \nabla_x T$  proportional to

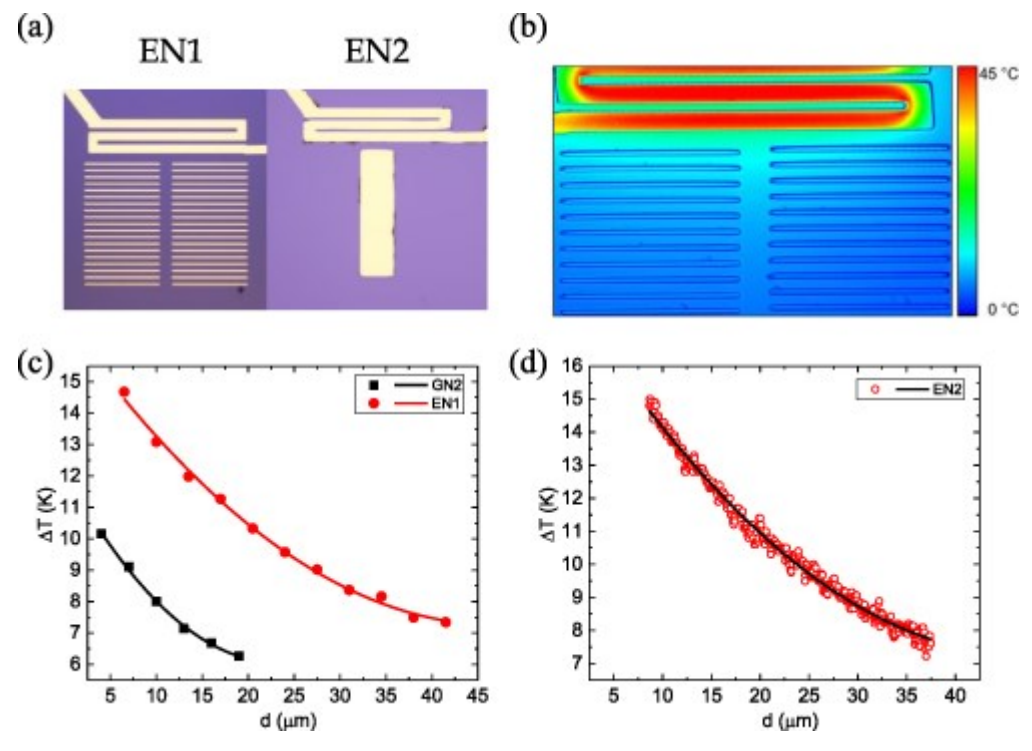
the local temperature gradient. As a result, the coefficient k provides a tool to monitor the local temperature gradient.

Figure 2(b) presents the magnetic field dependence of the Nernst voltage measured from different pairs of transverse electrodes. All the Nernst voltages increase linearly with increasing magnetic field, confirming that we are in a weak magnetic field regime ( $\mu B < 1$ ). It is clearly seen that the Nernst voltage measured from the transverse electrodes closer to the heater has a stronger field dependence, indicating a larger temperature gradient. We then plot the coefficient k as a function of the distance from the heater d in figure 2(c). As expected, the local temperature gradient is not constant but quite sensitive to the distance from the heater. It increases more than 50% when the distance is reduced from 26.5  $\mu$ m to 13  $\mu$ m. As a result, the calculated Nernst coefficient will strongly depend on the position of the measuring electrodes if the conventional linear-response approximation is utilized that the temperature gradient is constant along the channel. We have also done the measurements under different heating currents. Figure 2(d) shows the coefficient k as a function of the heating power, i.e. the square of the heating current. The dependence shows perfect linearity, confirming that the voltage comes from the Joule heating of the heater.

Since the micro-fabricated thermometers can only sense the local temperature, it seems that the failure of the linear-response approximation would make the estimation of the temperature gradient impossible. However, it is interesting to note that the temperature gradient shows quite good linear dependence on the distance from the heater (the deviation close to the heater will be discussed later). This linearity has also been observed in many other devices (see supplementary material). With this linear dependence, we can still extract the temperature gradient with enough accuracy from the temperature measurements with the micro-fabricated thermometers.

To confirm this linear dependence of the temperature gradient on the distance, we utilize the thermoreflectance measurements to map the temperature distribution with a better special resolution [27–30]. Thermoreflectance imaging technique can provide accurate temperature readings of the Au electrodes on the sample surface. We have done the thermoreflectance measurements in three devices, GN2, EN1, and EN2. GN2 is similar to GN1. Figure 3(a) shows the optical images of EN1 and EN2. EN1 has multiple pairs of transverse electrodes in parallel to the heater on a SiO2 substrate, while EN2 has a square gold film in stead. Figure 3(b) shows a typical thermoreflectance mapping measured in EN1 (see supplementary material). The temperature change  $\Delta T$  extracted from the variation of the thermoreflectance of the gold electrodes in GN2 and EN1 is presented in figure 3(c). Note that the  $\Delta T$  measured in GN2 is different from the one in EN1, due to the different heating

powers. In EN2,  $\Delta T$  is extracted from the variation of the thermoreflectance of the gold film along the middle line, shown in figure  $\underline{3}(d)$ .



Zoom In Zoom Out Reset image size

**Figure 3.** Thermoreflectance results. (a) Optical images of EN1 and EN2. (b) Thermoreflectance mapping of temperature in device EN1 with a current passing through the heater. From the thermoreflectance, temperature change can be determined. The colorbar shows the temperature difference with blue as zero and red as 45 °C. (c) Position dependence of the temperature change of the gold electrodes measured in GN2 and EN1. The electrodes in these two devices are separated lines. (d) Position dependence of the temperature change of the gold film in EN2. The solid lines in (c) and (d) show the parabolicly fittings.

It is clearly seen that the dependence of  $\Delta T$  on the distance from the heater is not a linear function. Consequently, the temperature gradient cannot be a constant but is

position-dependent. We then fit the data to a parabolic function,  $\Delta T = A(d-B)^2 + C$ 

, where A, B, and C are the fitting parameters. The parabolic fittings well match the data. The local temperature gradient is the derivative of  $\Delta T$ , thus a linear function of the distance from the heater. Hence, the thermoreflectance measurements confirm that the temperature gradient linearily depends on the distance from the heater.

The linear dependence of the temperature gradient can be well captured by a simple model which treat the heat transport as 2D. A heater is located at the center of a square area. The temperature at the edge of the square is set to be a constant, e.g. 300 K. Since the heater is made of gold, the temperature of the heater is assumed to be uniform.

The heater dimension is set to be 1  $\mu$ m in width and 100  $\mu$ m in length, similar to the heater in real devices. The heat dissipation through air and radiation is neglected since the measurements are performed in a high vacuum. Moreover, the gold electrodes and sample flakes on the surface are also neglected. The reason is that according to the similar thermoreflectance results from EN1 and EN2, the thermal transport is dominated by the substrate. Figure  $\underline{4}$ (a) presents the temperature distribution in the device. The isotherms are not equally spaced. Along the perpendicular bisector of the heater, figure  $\underline{4}$ (b) plots the temperature against the distance away from the heater denoted by d (see supplementary material). It is easy to find its similarity to the thermoreflectance results. The temperature change drops fast as the distance from the

heater increases. We then plot the magnitude of the temperature gradient,  $\frac{d\Gamma}{dx}$ , in figure  $\underline{4}$ (c). It is obvious that the temperature gradient is not a constant but shows a linear dependence on the distance from the heater in a quite large range, roughly from  $10~\mu\text{m}$  to  $40~\mu\text{m}$ .

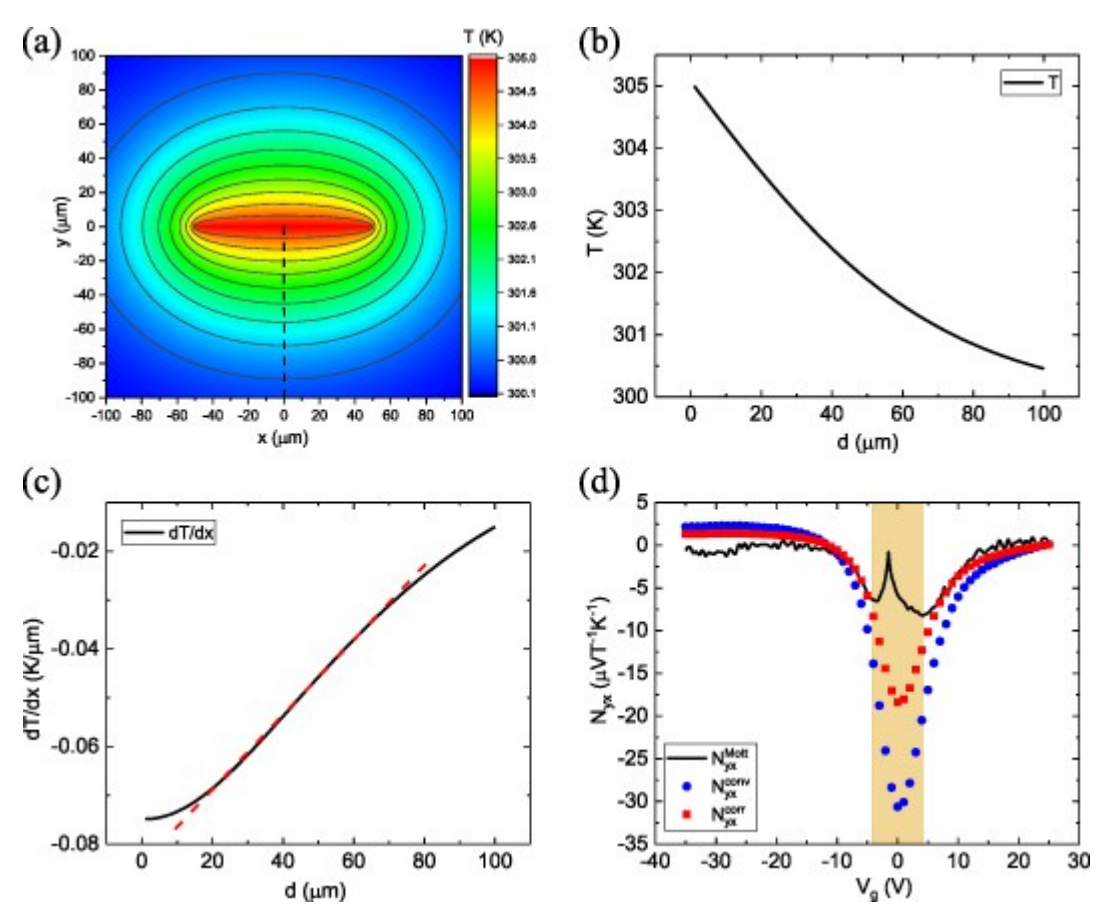


**Figure 4.** Simulations and comparing with Mott's formula. (a) Temperature distribution in the device. A zoom-in view with the range from  $-100\,\mu\mathrm{m}$  to  $100\,\mu\mathrm{m}$  (b) and (c) plot the temperature and temperature gradient as a function of the distance from the heater along the dash line in (a), respectively. The dash line in (c) is a guide line to the linear range of the temperature gradient. (d) Nernst coefficients measured in a single-layer graphene device. The square dots

represent the Nernst coefficient calculated with the corrected temperature gradient,  $N_{yx}^{corr}$ . The circular dots represent the Nernst coefficient calculated with the

average temperature gradient  $\frac{\Delta T}{L}$ ,  $N_{yx}^{conv}$ . The solid line shows the Nernst coefficient

deduced from the generalized Mott's formula,  $N_{yx}^{Mott}$ . Obviously, the corrected Nernst coefficient agrees much better with the value from the Mott's formula. It should be noted that the Mott's formula is not applicable in the vicinity of the Dirac point, denoted by the colored area in (d). The reason is that, due to the charge impurities from the substrate, there are always electron–hole puddles in real device. Consequently, two charge-carrier bands contribute to the electrical and thermoelectric transport when the chemical potential is tuned to the vicinity of the Dirac point. However, the Mott's formula considers only one band which has zero density of state at the Dirac point. Therefore, it is only applicable when the chemical potential is tuned away from this electron–hole-puddle regime.

We should mention that the linearity of the temperature gradient is accurate in a certain range. According to our results, the linearity of the temperature gradient maintains well in the range between  $10~\mu\text{m}$  and  $40~\mu\text{m}$ , a typical length scale for 2D devices. This range is actually proportional to the length of the heater. In our presented devices, the length of the heater is  $100~\mu\text{m}$ . Thus, the range of linearity is roughly 10%-40% of the heater length. If the size of the sample is larger than the above value, the length of the heater needs to be extended to make sure that the sample fits in the range. In figure  $\underline{4}(c)$ , it is also interesting to note that the temperature gradient shows saturation when the distance from the heater is small, as observed in figure  $\underline{2}(c)$ . This behavior can be understood that, when the distance from the heater is much smaller than the length of the heater, the heater can be approximated to be infinite long that the thermal transport goes back to one-dimensional.

Therefore, our systematic study provides several solutions to evaluate local temperature gradient within the standard geometry, although it cannot be directly detected. First, with knowing the length of the channel and the location of the electrodes, the local temperature gradient at the position where the Nernst voltage is measured can be calculated based on the linear dependence. Then, the Nernst coefficient can be deduced from this corrected temperature gradient. We followed this procedure to determine the Nernst coefficient of a single-layer graphene sample, the one shown in figure 1(b), and compare it to the value deduced from the generalized Mott relation. The generalized Mott formula relates the thermoelectric coefficient to

Mott relation. The generalized Mott formula relates the thermoelectric coefficient to  $S_{ij} = -\frac{\pi^2 k_B^2 T}{3|e|} \sum_k \left(\sigma^{-1}\right)_{ik} \left(\frac{\partial \sigma}{\partial \varepsilon_F}\right)_{kj} \ , \ \text{where} \ \sigma_{ij} \ \text{is the conductivity tensor,} \ \mathcal{E}_F \ \text{the Fermi energy, and} \ \boldsymbol{i}, \ \boldsymbol{j} \ \text{represent the} \ \boldsymbol{x} \ \text{and} \ \boldsymbol{y} \ \text{components}$  [23]. From the definition, the transverse thermoelectric coefficient is  $S_{yx} = N_{yx}B$ . Figure  $\underline{4}(d)$  shows the final results. The Nernst voltage is measured from the pair of transverse electrode cloest to the heater. We evaluate the Nernst coefficient with the

average temperature gradient  $\frac{\Delta T}{L}$  as conventional, denoted as  $N_{yx}^{\text{conv}}$ . We also calculate the corrected one,  $N_{yx}^{\text{corr}}$ , with the local temperature gradient calculated based on the linear dependence. It is obvious that  $N_{yx}^{\text{corr}}$  has a much better agreement with the value deduced from the generalized Mott relation. Second, as a special case, the temperature gradient in the middle of the channel equals the average temperature gradient  $\frac{\Delta T}{L}$ . Hence, one can measure the Nernst voltage in the middle of the channel and directly calculate the Nernst coefficient with the average temperature gradient. Last, as aforementioned, the temperature gradient saturates towards the heater. Therefore, linear-reponse approximation is still applicable as long as the channel locates in the saturation range which is roughly within 10% of the heater length. In practice, however, it requires a long heater and a short channel, which might raise difficulties to the device fabrications.

#### 4. Conclusion

In summary, we systematically study evaluating the temperature gradient in the Nernst measurements of 2D materials. With thermoelectric transport and thermoreflectance measurements, the temperature gradient on a substrate is shown to be position-dependent, suggesting that the long-adopted linear-reponse assumption is not accurate. Fortunately, the temperature gradient distribution can be well described by a linear function. The experimental results are well captured by simulations based on a simple 2D heat transport model. According to our results, although the local temperature gradient is not a constant, the measurement of the Nernst coefficient within the the standard geometry is still possible, as long as the temperature gradient is corrected considering the linear dependence. Our study provides solutions for accurate measurement of the Nernst coefficient and would be helpful for further studies of the Nernst effect of the 2D materials.

## Acknowledgments

This work is supported by the National Key R&D Program of China (Grant Nos. 2020YFA0308800 and 2019YFA0308402), the Beijing Natural Science Foundation (Z190006), the National Natural Science Foundation of China (Grant No. 61804008), the Strategic Priority Research Program of Chinese Academy of Sciences (Grant No. XDB30000000). T Z and M Z acknowledge the support from the National Science Foundation (Grant No. 1653268). J D acknowledges Shucheng Duan for fruitful discussion.

# Data availability statement

The data that support the findings of this study are available upon reasonable request from the authors.

#### References

- 1. Bell, L. E. Science 2008, 321, (5895), 1457.
- 2. Snyder, G. J.; Toberer, E. S. Nat Mater 2008, 7, (2), 105-114.
- 3. Mao, J.; Chen, G.; Ren, Z. Nat Mater 2021, 20, (4), 454-461.
- 4. Hicks, L. D.; Dresselhaus, M. S. Phys Rev B 1993, 47, (19), 12727-12731.
- 5. Poudel, B.; Hao, Q.; Ma, Y.; Lan, Y.; Minnich, A.; Yu, B.; Yan, X.; Wang, D.; Muto, A.; Vashaee, D.; Chen, X.; Liu, J.; Dresselhaus, M. S.; Chen, G.; Ren, Z. *Science* **2008**, 320, (5876), 634.
- 6. Ortega, S.; Ibáñez, M.; Liu, Y.; Zhang, Y.; Kovalenko, M. V.; Cadavid, D.; Cabot, A. *Chemical Society Reviews* **2017**, 46, (12), 3510-3528.
- 7. Ibáñez, M.; Luo, Z.; Genç, A.; Piveteau, L.; Ortega, S.; Cadavid, D.; Dobrozhan, O.; Liu, Y.; Nachtegaal, M.; Zebarjadi, M.; Arbiol, J.; Kovalenko, M. V.; Cabot, A. *Nature Communications* **2016**, 7, (1), 10766.
- 8. Shi, X.-L.; Zou, J.; Chen, Z.-G. Chemical Reviews 2020, 120, (15), 7399-7515.
- 9. Zhao, L.-D.; Lo, S.-H.; Zhang, Y.; Sun, H.; Tan, G.; Uher, C.; Wolverton, C.; Dravid, V. P.; Kanatzidis, M. G. *Nature* **2014**, 508, 373.
- 10. Zhao, L.-D.; Tan, G.; Hao, S.; He, J.; Pei, Y.; Chi, H.; Wang, H.; Gong, S.; Xu, H.; Dravid, V. P.; Uher, C.; Snyder, G. J.; Wolverton, C.; Kanatzidis, M. G. *Science* **2015**.
- 11. Kim, D.; Syers, P.; Butch, N. P.; Paglione, J.; Fuhrer, M. S. Nano Lett 2014, 14, (4), 1701-1706.
- 12. Yoshida, M.; Iizuka, T.; Saito, Y.; Onga, M.; Suzuki, R.; Zhang, Y.; Iwasa, Y.; Shimizu, S. *Nano Lett* **2016**, 16, (3), 2061-2065.
- 13. Zuev, Y. M.; Chang, W.; Kim, P. Phys Rev Lett 2009, 102, (9), 096807.
- 14. Saito, Y.; Iizuka, T.; Koretsune, T.; Arita, R.; Shimizu, S.; Iwasa, Y. Nano Lett 2016, 16, (8), 4819-4824.
- 15. Wu, J.; Chen, Y.; Wu, J.; Hippalgaonkar, K. Advanced Electronic Materials 2018, 4, (12), 1800248.
- 16. Duan, J.; Wang, X.; Lai, X.; Li, G.; Watanabe, K.; Taniguchi, T.; Zebarjadi, M.; Andrei, E. Y. *Proceedings of the National Academy of Sciences* **2016**, 113, (50), 14272-14276.
- 17. Dehkordi, A. M.; Zebarjadi, M.; He, J.; Tritt, T. M. Materials Science and Engineering: R: Reports 2015, 97, 1-22.
- 18. Sakuraba, Y. Scripta Materialia 2016, 111, 29-32.
- 19. Ikhlas, M.; Tomita, T.; Koretsune, T.; Suzuki, M.-T.; Nishio-Hamane, D.; Arita, R.; Otani, Y.; Nakatsuji, S. *Nat Phys* **2017**, 13, 1085.
- 20. Mizuguchi, M.; Nakatsuji, S. Science and Technology of Advanced Materials 2019, 20, (1), 262-275.
- 21. Xiao, D.; Yao, Y.; Fang, Z.; Niu, Q. Phys Rev Lett 2006, 97, (2), 026603.

- 22. Xiao, D.; Chang, M.-C.; Niu, Q. Reviews of Modern Physics 2010, 82, (3), 1959-2007.
- 23. Wenjie Zhang, P. W., Brian Skinner, Ran Bi, Vladyslav Kozii, Chang-Woo Cho, Ruidan Zhong, John Schneeloch, Dapeng Yu, Genda Gu, Liang Fu, Xiaosong Wu, Liyuan Zhang. *ArXiv* **2019**, arXiv:1904.02157.
- 24. Zhang, W.; Wang, P.; Skinner, B.; Bi, R.; Kozii, V.; Cho, C.-W.; Zhong, R.; Schneeloch, J.; Yu, D.; Gu, G.; Fu, L.; Wu, X.; Zhang, L. *Nature Communications* **2020**, 11, (1), 1046.
- 25. Narita, H.; Ikhlas, M.; Kimata, M.; Nugroho, A. A.; Nakatsuji, S.; Otani, Y. *Appl Phys Lett* **2017**, 111, (20), 202404.
- 26. Federico Caglieris, C. W., Steffen Sykora, Vicky Süss, Chandra Shekhar, Claudia Felser, Bernd Büchner, Christian Hess. *ArXiv* **2018**, arXiv:1805.09286.
- 27. Sakai, A.; Mizuta, Y. P.; Nugroho, A. A.; Sihombing, R.; Koretsune, T.; Suzuki, M.-T.; Takemori, N.; Ishii, R.; Nishio-Hamane, D.; Arita, R.; Goswami, P.; Nakatsuji, S. *Nat Phys* **2018**.
- 28. Guin, S. N.; Manna, K.; Noky, J.; Watzman, S. J.; Fu, C.; Kumar, N.; Schnelle, W.; Shekhar, C.; Sun, Y.; Gooth, J.; Felser, C. *NPG Asia Materials* **2019**, 11, (1), 16.
- 29. Yang, H.; You, W.; Wang, J.; Huang, J.; Xi, C.; Xu, X.; Cao, C.; Tian, M.; Xu, Z.-A.; Dai, J.; Li, Y. *Physical Review Materials* **2020**, 4, (2), 024202.
- 30. Wang, Y.; Li, L.; Ong, N. P. Phys Rev B 2006, 73, (2), 024510.
- 31. Hu, J.; Caputo, M.; Guedes, E. B.; Tu, S.; Martino, E.; Magrez, A.; Berger, H.; Dil, J. H.; Yu, H.; Ansermet, J.-P. *Phys Rev B* **2019**, 100, (11), 115201.
- 32. Small, J. P.; Perez, K. M.; Kim, P. Phys Rev Lett 2003, 91, (25), 256801.
- 33. Checkelsky, J. G.; Ong, N. P. Phys Rev B 2009, 80, (8), 081413(R).
- 34. Wei, P.; Bao, W. Z.; Pu, Y.; Lau, C. N.; Shi, J. Phys Rev Lett 2009, 102, (16), 166808.
- 35. Rana, K. G.; Dejene, F. K.; Kumar, N.; Rajamathi, C. R.; Sklarek, K.; Felser, C.; Parkin, S. S. P. *Nano Lett* **2018**, 18, (10), 6591-6596.
- 36. Xu, J.; Phelan, W. A.; Chien, C.-L. Nano Lett 2019, 19, (11), 8250-8254.
- 37. Christofferson, J.; Shakouri, A. Review of Scientific Instruments 2005, 76, (2), 024903.
- 38. Farzaneh, M.; Maize, K.; Lüerßen, D.; Summers, J. A.; Mayer, P. M.; Raad, P. E.; Pipe, K. P.; Shakouri, A.; Ram, R. J.; Hudgings, J. A. *Journal of Physics D: Applied Physics* **2009**, 42, (14), 143001.
- 39. Chatterjee, B.; Dundar, C.; Beechem, T. E.; Heller, E.; Kendig, D.; Kim, H.; Donmezer, N.; Choi, S. *Journal of Applied Physics* **2020**, 127, (4), 044502.
- 40. Zhu, T.; Olson, D. H.; Hopkins, P. E.; Zebarjadi, M. Review of Scientific Instruments 2020, 91, (11), 113701.

# **Figures**

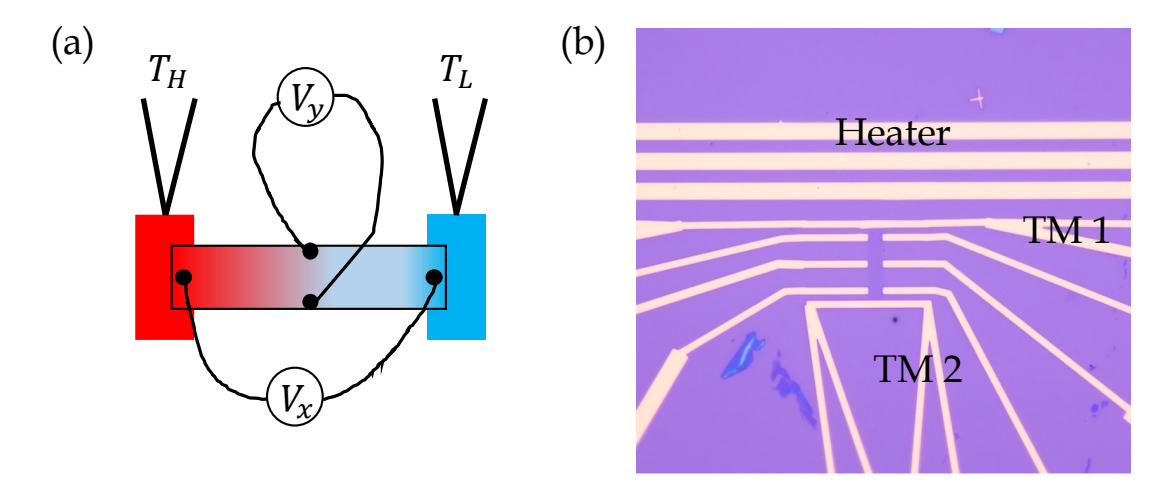


Figure 1. Thermoelectric measurement setup for macro- and microscopic devices. (a) For macroscopic devices, the sample is placed in a vacuum with the ends attached to the heating stage ( $T_H$ ) and cold sink ( $T_L$ ), respectively. The longitudinal and transverse electrodes can measure the Seebeck and Nernst voltages simultaneously. (b) The standard geometry is widely used for thermoelectric measurements on microscopic devices. Thick gold wires serve as the heater. TM1 and TM2 are two thin wires which can monitor the local temperature by four-probe measurements.

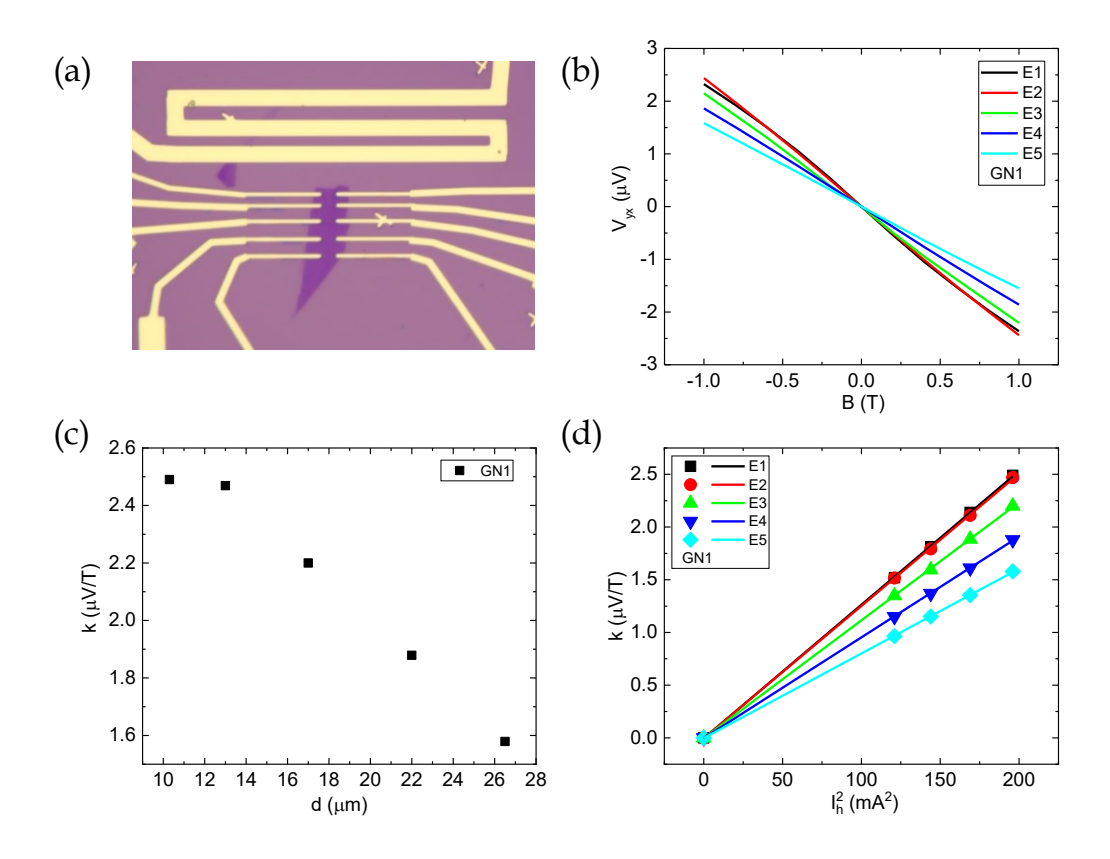


Figure 2. Thermoelectric measurements on multilayer graphene. (a) Optical image of the device GN1. The device has multiple transverse electrodes to detect the Nernst voltage at different locations. (b) Magnetic field dependence of Nernst voltages measured by different pairs of transverse electrodes. (c) The position dependence of the coefficient k. (d) The coefficient k shows a very good linear dependence on the heating power in the heater.

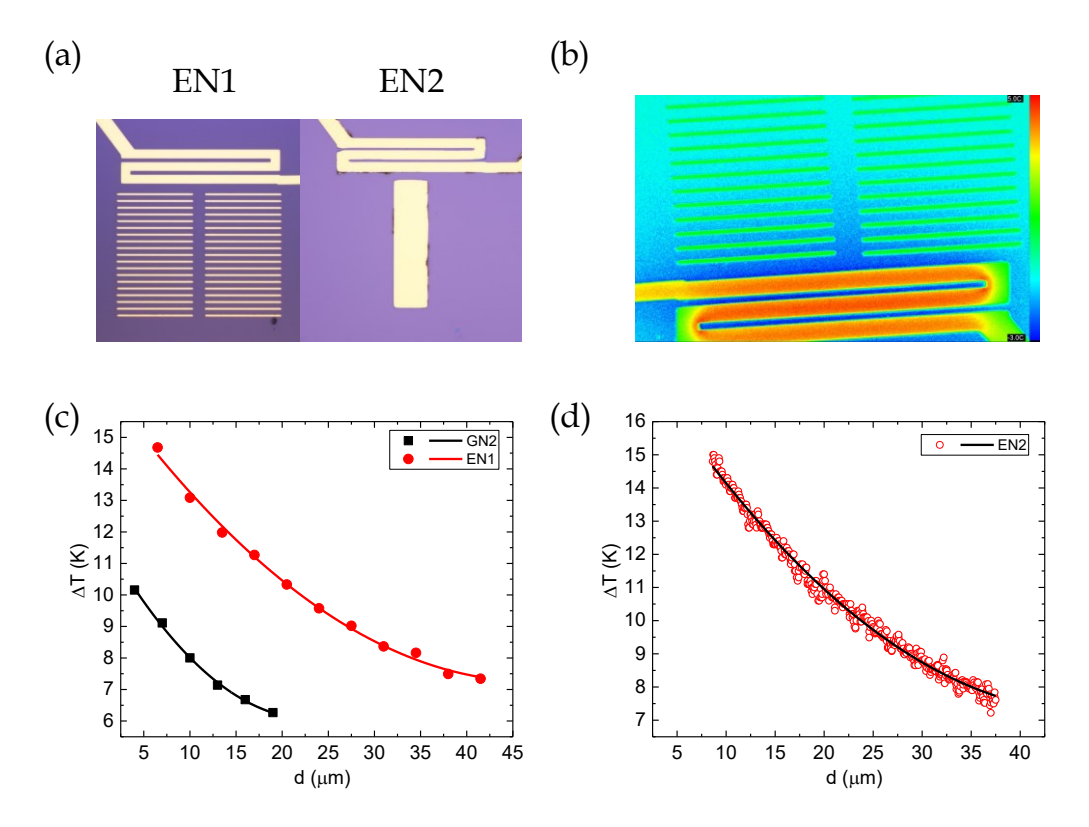


Figure 3. Thermoreflectance measurements on multiple devices. (a) Optical images of EN1 and EN2. (b) Thermoreflectance mapping of device EN1 with a current passing through the heater. From the thermoreflectance, temperature change can be determined. The colorbar shows the temperature with blue as zero and red as 45 °C temperature difference. (c) Position dependence of the temperature change of the gold electrodes measured in GN2 and EN1. The electrodes in these two devices are separated lines. (d) Position dependence of the temperature change of the gold film in EN2. The solid lines in (c) and (d) show the results of the parabolic fitting.

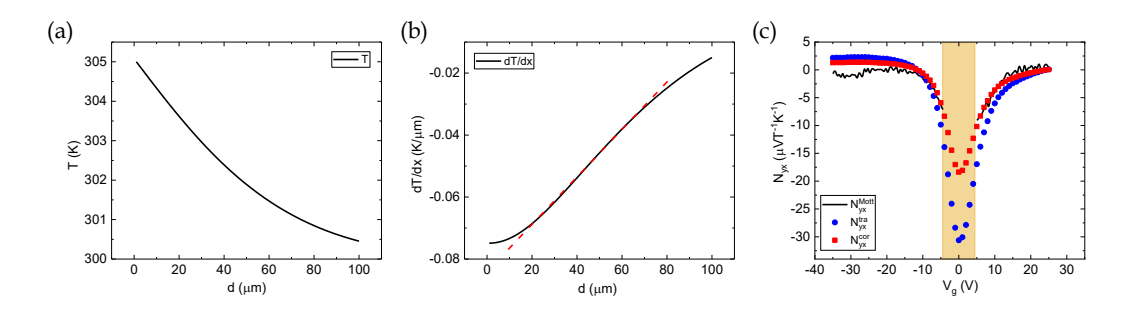


Figure 4. Simulated temperature distribution and Nernst coefficient comparing to Mott's relation. (a) and (b) plot the temperature and temperature gradient distributions, respectively, calculated from a simple model. The dash line in (b) is a guide line to the linear range of the temperature gradient. (c) Nernst coefficients measured in a single-layer graphene device. The square dots represent the Nernst coefficient calculated with the corrected temperature gradient,  $N_{yx}^{cor}$ . The circular dots represent the Nernst coefficient calculated with the average temperature gradient  $\frac{\Delta T}{L}$ ,  $N_{yx}^{tra}$ . The solid line shows the Nernst coefficient deduced from the generalized Mott's formula,  $N_{yx}^{Mott}$ . Obviously, the corrected Nernst coefficient agrees much better with the value from the Mott's formula. It should be noted that the Mott's formula is not applicable in the vicinity of the Dirac point, denoted by the colored area in (c). The reason is that, due to the charge impurities, there are always electron-hole puddles in real device. Consequently, two charge-carrier bands contribute to the electrical and thermoelectric transport when the chemical potential is tuned to the vicinity of state at the Dirac point. However, the Mott's formula considers only one band which has zero density of state at the Dirac point. Therefore, it is only applicable when the chemical potential is tuned away from this electron-hole-puddle regime.